SAND2015-4280C

Temporal Evolution of Turbulent Eddies in a Compressible Jet in Crossflow Measured using Pulse-Burst PIV

Steven J. Beresh,[1] Justin L. Wagner,[2] John F. Henfling,[3] Russell W. Spillers,[4] and Brian O. M. Pruett[5]
Sandia National Laboratories, Albuquerque, NM, 87185

Pulse-burst PIV has been employed to acquire time-resolved data at 25 kHz of a supersonic jet exhausting into a subsonic compressible crossflow. Data were acquired along the windward boundary of the jet mixing layer with the freestream and can be used to identify the turbulent eddies as they convect downstream in the far-field of the interaction. Eddies were found to have a tendency to occur in closely-spaced counter-rotating pairs and are routinely observed in the PIV movies, but the variable orientation of these pairs plus interactions between different eddies makes them difficult to detect in a statistical sense. Correlated counter-rotating vortices are more strongly observed to pass by at a spacing about three times the separation between paired vortices, both leading and trailing the reference eddy. This indicates the paired nature of the turbulent eddies and the tendency for these pairs to convect through the field of view at uniform spacings. Velocity spectra reveal a peak at a frequency consistent with this larger spacing between shear-layer vortices rotating with identical sign.

Introduction

In recent years, time-resolved particle image velocimetry (TR-PIV) has evolved as a means of measuring temporally correlated velocity fields, allowing the acquisition of PIV movies to add a time component to fluid dynamics investigations. Whereas TR-PIV has emerged in a variety of low-speed flows as an adaptation of PIV technology using diode-pumped solid-state kHz-rate lasers and fast CMOS cameras, the requirements of high-speed flows exceed the capabilities of these technologies. Instead, TR-PIV in high-speed flows is best accomplished using a pulse-burst laser, as this is the only light source capable of producing sufficient energy at the necessarily rapid pulse rates, though with the penalty of a very low duty cycle. Simultaneous with the maturation of pulse-burst laser technology, quality high-speed cameras have begun to achieve desirable framing rates without excessive sacrifice of the size of the spatial array. Pulse-burst PIV has a minimal history. Wernet appears to have been the first to achieve pulse-burst PIV [1], with more recent development offered by Brock et al [2] and Miller et al [3,4]. Pulse-burst PIV had not seen application in a wind tunnel or other testing facility until Beresh et al demonstrated its use in a transonic wind tunnel [5].

Studies of turbulence in high-speed flows will benefit greatly from pulse-burst PIV's addition of a time-component to full-field velocimetry. One such example would be a supersonic jet exhausting into a subsonic compressible crossflow, studied at considerable length by Beresh et al using conventional PIV [6-8]. In particular, Ref. [7] examined the typical behavior of the turbulent eddies comprising the jet interaction. However, the PIV diagnostic in use at the time could only assess characteristic behavior of the turbulent eddies by conditionally averaging numerous velocity fields at different downstream positions. Pulse-burst PIV, on the other hand, can

[1]Distinguished Member of the Technical Staff, Engineering Sciences Center, AIAA Associate Fellow, correspondence to: P.O. Box 5800, Mailstop 0825, (505) 844-4618, email: sjberes@sandia.gov
[2]Senior Member of the Technical Staff, AIAA Senior Member
[3]Distinguished Technologist, AIAA Senior Member
[4]Principal Technologist
[5]Senior Technologist

This work is supported by Sandia National Laboratories and the United States Department of Energy. Sandia is a multiprogram laboratory managed and operated by Sandia Corporation, a wholly owned subsidiary of Lockheed Martin Corporation, for the United States Department of Energy's National Nuclear Security Administration under contract DE-AC04-94AL85000.

temporally track each turbulent eddy and therefore directly follow its evolution as it convects downstream. The first demonstration of pulse-burst PIV in a wind tunnel [5] captured the turbulent eddies along the windward shear layer in the far-field of the interaction as the jet mixed with the crossflowing freestream, but were not studied in sufficient depth to elucidate the fluid dynamics of turbulent eddies in this mixing application.

Numerous vortical structures have been identified in jet-in-crossflow interactions and they recently have been ably reviewed by Karagozian [9] and Mahesh [10]. Amongst these features are the shear layer vortices, which are observed instantaneously but have no representation in the mean flowfield other than their influence on mixing. The shear layer vortices originate from the Kelvin-Helmholtz instability as the jet first begins mixing with the crossflow, then follow the windward boundary of the jet as it turns over and begins to realign with the freestream (e.g., [11, 12]). Low-speed experiments indicate that these shear-layer vortices have a prominent role in the formation of the counter-rotating vortex pair (CVP) in the near-field, but once the CVP is established in the far-field, they play a considerably reduced role in the continued production of turbulence and alter the scaling characteristics of the decaying jet [13-15]. The experiments of Megerien et al [16] and Getsinger et al [17] show that the frequency associated with the Kelvin-Helmholtz instability is distinct in the near-field but no preferred frequency is found in the far-field, a result supported by the stability analysis of Alves et al [18].

Although compressible jet-in-crossflow interactions qualitatively maintain the same features as their low-speed counterparts, accumulating evidence suggests that there are differences in the windward shear layer vortices that affect the downstream growth of the interaction. Several experiments have shown that the large turbulent eddies associated with the windward shear layer are much more persistent downstream for high-speed jets in crossflow and have a more dominant presence [19-21], an observation supported by several Large-Eddy Simulations (LES) [22-24]. This appears to be because the shock structure emanating from the jet nozzle exit is unsteady and deflections of it allow high-speed fluid from the jet to escape into the crossflow with minimal deceleration, altering the formation of the shear-layer vortices in comparison with the dominance of the Kelvin-Helmholtz instability at low speeds [22, 24-27]. This alters the role of the shear layer vortices in the far-field of the interaction and appears to give them a prominence comparable to the CVP. Ben-Yakar et al [20] indicate that they appear uniformly spaced in the far-field whereas VanLerberghe et al [25] indicate that their periodicity is reduced. Regardless, these observations suggest that the windward shear layer vortices play an enhanced role in the far-field behavior of the jet interaction for a compressible flow in comparison to a low-speed flow.

The present work aims to utilize the pulse-burst PIV data that were acquired by Beresh et al [5] to demonstrate the new measurement capabilities, but here analyze them to evaluate the behavior of the shear-layer eddies in the far-field of a compressible jet in crossflow. These data offer an opportunity to examine the temporal behavior of these eddies, which has not previously been available for a high-speed flow, and compare it to the better known behavior at low speeds. This can help determine whether the interaction develops differently for a compressible jet.

Experimental Apparatus

Experiments were conducted in Sandia's Trisonic Wind Tunnel (TWT) at Mach 0.8. The TWT is a blowdown-to-atmosphere facility using air as the test gas. In its solid-wall transonic configuration, the test section is a straightforward rectangular duct of dimensions 305 × 305 mm^2 (12 × 12 $inch^2$) and any Mach number between 0.5 and about 0.9 may achieved by adjusting the area of a downstream throat. Mach 0.8 was tested exclusively for the data used herein with a stagnation pressure of 154 kPa and a fixed stagnation temperature of 321K ± 2K. The test section is enclosed within a pressurized plenum to accommodate ventilated test sections for other tunnel configurations.

The experiment was configured with a supersonic jet positioned on the top wall of the transonic test section upstream of the windows, as seen in Fig. 1. The upstream location of the jet positioned the imaging region for measurement of the far-field of the jet once it has developed. The laser sheet was introduced through a window in the floor of the test section as well as a matching window in the lower wall of the TWT plenum. It was oriented in the streamwise plane and

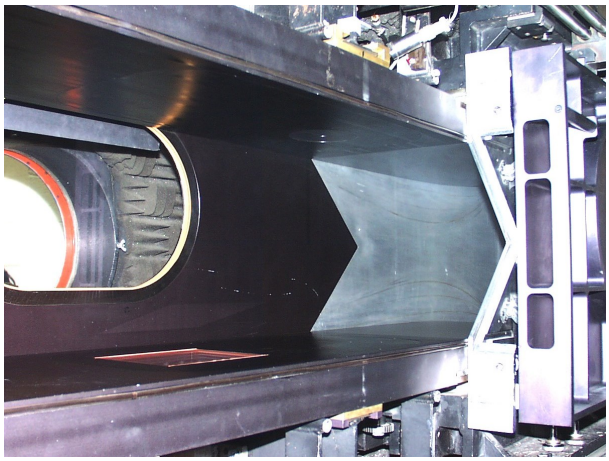

Fig. 1: The jet hardware installed into the solid-wall transonic test section of the Trisonic Wind Tunnel.

aligned to the center plane of the test section, which coincides with the center of the jet nozzle exit. A nitrogen jet exhausted from a conical nozzle with a design Mach number of 3.73, an expansion half-angle of 15 deg, and an exit diameter of 9.53 mm (0.375 inch). The nozzle was fit to a settling chamber designed for a maximum pressure of 14 MPa and instrumented to provide stagnation pressure and temperature measurements. In the present case, the jet was operated at two different conditions; one a pressure of 4.9 MPa to produce a jet-to-freestream dynamic pressure ratio of J=10.2 and the other a pressure of 3.9 MPa for J=8.1. This shifted the position of the jet relative to the imaging field of view, such that J=10.2 data were acquired nearer the core of the jet and J=8.1 farther into the outer mixing layer. The coordinate axes originate at the centerpoint of the nozzle exit plane; the u component is in the streamwise direction and v component is positive away from the top wall of the tunnel.

The TWT is seeded by a thermal smoke generator (Corona Vi-Count 5000) that produces a large quantity of particles typically 0.2 - 0.3 μm in diameter from a mineral oil base. Particles are delivered to the TWT's stagnation chamber upstream of the flow conditioning section through a series of pipes and tubes, in which agglomeration of the particles occurs. Previous measurement of the *in-situ* particle response across a shock wave generated by a wedge shows the particle size to be 0.7 - 0.8 μm. Stokes numbers have been estimated as at most 0.05 based on *a posteriori* analysis of PIV measurements, which is sufficiently small to rapidly attain the local velocity and reduce particle lag errors to a negligible level.

In the current work, a quasi-continuous burst-mode laser (QuasiModo-1000, Spectral Energies, LLC) with both diode- and flashlamp-pumped Nd:YAG amplifiers was used to produce a high-energy pulse train at 532 nm. The pulse-burst laser generates up to 10.2 ms duration bursts every 8 seconds with a maximum 532 nm pulse energy of 500 mJ at 5 kHz and 20 mJ pulse energy at its maximum repetition rate of 500 kHz. The laser is capable of producing doublets with variable interpulse spacing at all repetition rates, though in the present work the time between pulses in a doublet was 2.00 μs. In this work, 25 kHz doublets were used for PIV measurements with energy per pulse of 175 mJ for a 2.5 ms burst duration. The design of the pulse-burst laser is based on master oscillator power amplifier architecture and is similar to previously reported pulse-burst-mode lasers [28-30].

Images were acquired using two high-speed CMOS cameras (Photron SA-X2) which have a full framing rate of 12.5 kHz and an array of 1024 × 1024 pixels at this speed. Their windowing function allows the framing rate to be increased by sampling a semi-arbitrary portion of the imaging array. In the present case, each camera operated at 50 kHz with an array of 640 × 384 pixels. The two pulses in a doublet were frame-straddled around the cameras' interframe transfer time, which allowed cross-correlation analysis of pairs of images; thus PIV velocity fields were acquired at 25 kHz. The cameras each were equipped with 200-mm focal length lenses.

The two cameras were placed side by side to extend the field of view in the streamwise direction to track the convection of turbulent eddies, yielding a combined field of view of approximately 70 × 21 mm^2 for two-component PIV. Unfortunately, the large size of the camera bodies precluded placing them sufficiently close to one another to image the laser sheet from a normal direction. Therefore, they were canted at an angle of 5 deg such that their individual imaging regions were adjacent and could be combined for vector processing. This angle creates a perspective bias on the velocity vectors due to added sensitivity to the out-of-plane velocity component, but calculations estimate that the maximum induced error is no more than 2%. This was considered to be an acceptable compromise in order to create the desired field of view.

Data were processed using LaVision's DaVis v8.2. In each case, image pairs were background-corrected, intensity normalized, and then interrogated with an initial pass using 64 × 64 pixel interrogation windows, followed by two iterations of 24 × 24 pixel interrogation windows. A 50% overlap in the interrogation windows was used as well. The resulting vector fields were validated based upon signal-to-noise ratio, nearest-neighbor comparisons, and allowable velocity range. A single pass of light vector smoothing was employed as well.

Results and Discussion

A mean field of the vertical velocity component acquired from 1500 independent snapshots of a conventional 10-Hz PIV system is shown in Fig. 2 for the J=8.1 jet. These data were acquired prior to the pulse-burst PIV and were illuminated by a typical 10-Hz dual-cavity Nd:YAG laser rather than the pulse-burst laser and images were captured using low-speed PIV cameras (LaVision sCMOS). The coordinate axes were centered on the jet nozzle exit and the field of view was established downstream of the nozzle exit and at some distance from the wall to capture the core of the jet and its mixing interface with the freestream. The strength of the counter-rotating vortex pair is captured by the vertical velocity component and it can be seen to decay with downstream distance as the jet trajectory slowly moves it outward. The dashed rectangular box illustrates the position of the combined field-of-view of the high-speed cameras for the pulse-burst PIV, which is positioned to capture the turbulent eddies to be found at the windward mixing interface.

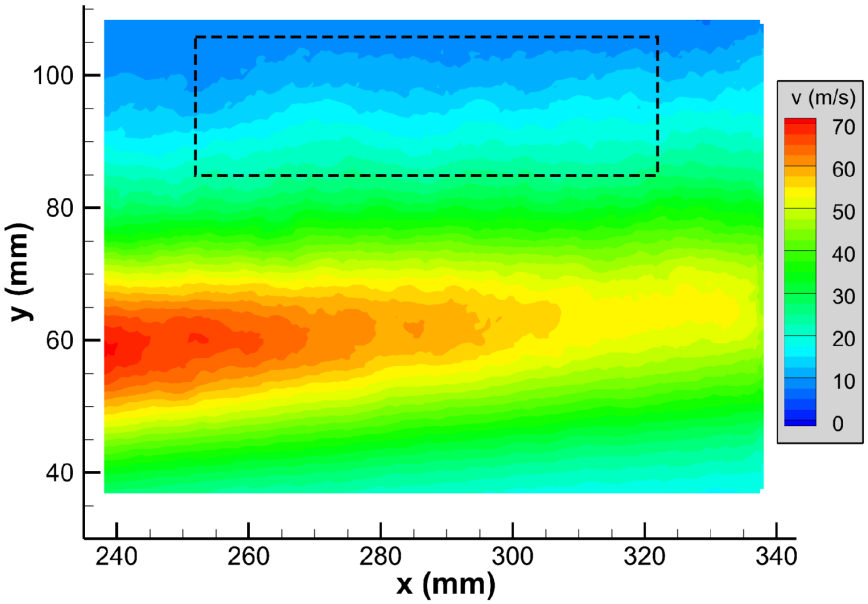

Fig. 2: Mean vertical velocity component of the jet in crossflow at J=8.1 acquired using a conventional 10-Hz PIV system. The dashed rectangular box illustrates the field of view of the pulse-burst PIV.

A sample velocity field sequence is shown in Fig. 3, acquired at 25 kHz using cross-correlation analysis. It was extracted from a much longer 2.5 ms burst duration and represents only an eight-snapshot, 280-µs portion of the full burst. Velocity fluctuations were found by calculating the mean velocity field over several wind tunnel runs and then subtracting it from each individual velocity field. The plot shows in-plane velocity fluctuations superposed on the derived vorticity field as a color contour and white contour lines denoting the swirl field.

Figure 3 shows a counter-rotating pair of eddies entering the field of view on the left edge. As the pair convects downstream, the two eddies can be seen to rotate with respect to one another as they simultaneously drift farther out in the y direction, reflecting the gradual trajectory of the jet. The paired vortices are separated by approximately 10 mm. A second, weaker pair of counter-rotating vortices can be seen to enter the field of view shortly behind the first pair, becoming visible at t=80 µs at the bottom of the frame. Their orientation is nearly horizontal whereas the first pair entered the field of view nearly vertically oriented. These vortices diffuse with downstream travel and become difficult to detect by t=200 µs. Yet another pair of counter-rotating eddies enters the field of view at t=160 µs and still another at t=240 µs, each with different rotational alignment. These paired eddies are characteristic of the entire data set, though their stability varies greatly. Some are like the first pair seen initially at t=0 µs in Fig. 3, remaining sharply defined as they convect and rotate. Others may shear one or both of the eddies into smaller eddies or diffuse vorticity, sometimes leading to a single well-defined vortex seen to remain stable and convect downstream intact. Interestingly, each of the eddies within a pair in Fig. 3 is separated by a reasonably consistent 8-10 mm. The distance between pairs is larger, about 20-30 mm.

A total of 61 bursts were acquired for J=10.2 and 53 bursts for J=8.1, each 2.5 ms in duration. While velocimetry movie sequences such as Fig. 3 can reveal exemplary behavior of the flow, statistical analysis across the entire data set is needed to show the range of behavior of turbulent eddies. As a first step, representative eddy behavior can be found by ensemble averaging the velocity field in a manner similar to that used in Beresh et al [7], except here the temporal behavior of the eddies may be revealed as well. To accomplish this, a window was created near the upstream edge of the field of view in which the center of the strongest eddy was located. Within the range of $254 \le x \le 262$ mm and $84 \le y \le 101$ mm, the position of maximum swirling strength was located to mark the center of the strongest eddy in the window, then the entire flow field was shifted to the mean position of these eddies over the entire data set. That is, the representative eddy found in the conditional window was repositioned such that their centers coincided at their mean center point. Once co-located, the vector fields were averaged to produce a representative large-scale eddy. The search procedure used signed swirl, in which the sign of the vorticity at the same location was assigned to the swirling strength to allow positive and negative rotation to be distinguished. A minimum threshold was required to establish the presence of an identifiable vortex.

Since the entire flowfield is repositioned based on the conditional eddy, including subsequent time steps, this allows the typical downstream evolution of the vortex to be recorded. However, the trajectory of each eddy varies

somewhat and the ensemble-averaged eddy will appear to quickly dissipate simply due to the varied eddy position. To rectify this, at each subsequent time step, the algorithm once again searches for the swirl peak (though limited to a nearby location) and re-centers the eddy location to the mean location. Therefore, the resulting ensemble-averaged characteristic eddy follows the mean trajectory downstream and displays any decay or distortion entirely due to the eddy's evolution in time and not variation in position.

Figure 4 shows the ensemble-averaged mean turbulent eddy behavior conditioned on a negative-rotating eddy, displayed on the same scale as the sequence of instantaneous velocity fields in Fig. 3. As the eddy convects downstream, its strength can be seen to gradually diminish, as indicated by both the magnitude of the vorticity field and the length of the velocity vectors. It also is evident that the ensemble-averaged rotation is not uniform, with stronger velocity vectors seen on the upstream side of the eddies as compared to their downstream side. Or viewed differently, velocities have greater magnitudes pointed away from the wall than pointed towards it. At first glance, this may be attributed to superposition of the outward trajectory of the jet, which would enhance vectors aligned to the $+y$ direction and diminish those aligned to $-y$. This cannot be the case, however, as the effects of the jet trajectory would have been removed when the mean velocity field was subtracted to obtain the fluctuating velocity fields.

The ensemble-averaged eddies of Fig. 4 do not reproduce the pairs of eddies commonly seen in the instantaneous data such as that of Fig. 3, in which counter-rotating vortices are often seen separated by about 8-10 mm. This suggests that the orientation of these paired vortices is random and evenly distributed, which causes it to average out in Fig. 4 and therefore a paired vortex cannot be found. However, a closer examination of Fig. 4 reveals that a diffuse positive-rotating vortex leads the conditional negative vortex by about 30 mm and a similar diffuse positive vortex trails trails it by about 25 mm. These spacings appear roughly consistent with the repetition of paired eddies observed in Fig. 3. This suggests that opposite-signed vortices tend to recur at a separation of about 25-30 mm during the mixing of the jet into the crossflow. The repeatability and spacing of these eddies must possess significant variability since the conditional vortex is so diffuse and weak.

Ensemble averages of positive-rotating eddies are given in Fig. 5. Similar to the negative vortex of Fig. 4, the velocity field is nonuniform, though differently than in Fig. 4. Here, vectors are stronger on the downstream side of the vortex, which again is oriented away from the wall. A negatively-rotating vortex is seen more clearly about 20 mm downstream of the conditional positive vortex, which identifies the strong velocity magnitudes away from the wall as the upwash between two counter-rotating vortices.

The nonuniform ensemble-averaged vortices can be explained by considering the turbulent eddies as pairs. The movie sequence of Fig. 3 clearly shows a tendency for turbulent eddies to occur as counter-rotating pairs separated by about 8-10 mm. These pairs then tend to recur every 25-30 mm, also evident in Fig. 3 and suggested by the ensemble averages of Figs. 4 and 5. The contribution from a counter-rotating complement to a vortex leads to greater velocity magnitudes in the upwash between them and this creates the nonuniformity seen in Figs. 4 and 5. It is much like the mean velocity field produced by the CVP. The paired vortex that serves as a counterpart to the conditional vortices is faint in the ensemble averages because its position and strength and perhaps even the probability of its presence varies in time.

To better visualize the presence of paired turbulent eddies, the ensemble-average velocity fields of Figs. 4c and 5c have been recast in Fig. 6 with altered velocity and vorticity scales. Here, all velocity vectors are a uniform length and the vorticity scales have been decreased by an order of magnitude, both changes meant to emphasize the weakly-correlated vortices that were difficult to discern in Figs. 4 and 5. Furthermore, the instantaneous location of the nearest paired vortex is shown by the scatter plot of white data points. Throughout the data set, once the position of the conditional vortex was identified, the nearest vortex of opposite sign was located as well. The same minimum threshold was required as for the conditional vortex. The cloud of data points therefore depicts the location of the counterpart in the pair of turbulent eddies so commonly seen in the movie of Fig. 3 and allows a sense of its orientation at any given moment in time.

Figure 6 indicates that the paired vortex in fact can be seen at a separation consistent with 8-10 mm, but it is weak in the ensemble averages. On a reduced vorticity scale, it becomes visible but is diffuse due to its variation in position. The cloud of data points representing the instantaneous position of the paired vortex indicates that it can be found at any azimuthal position surrounding the conditional vortex, but there is a weak preference for a position such that the negative vortex leads the positive vortex as they convect downstream. This orientation accelerates fluid away from the wall between the two eddies. The paired vortex is not evident in the velocity field. Conversely, the uniform-length vectors clearly reveal correlated vortices at a separation of 20-30 mm. In Fig. 6a, a correlated vortex is seen leading the conditional negative vortex by about 30 mm, with another correlated vortex following behind by a little more than 20 mm. Similarly, Fig. 6b shows a leading correlated vortex by 20 mm and a noisy trailing vortex just entering the field of view nearly 30 mm behind. Therefore, Fig. 6 visualizes the presence of both

the paired nature of the turbulent eddies and the tendency for these pairs to convect through the field of view at uniform spacings.

Another way to study the pulse-burst PIV data is to perform cross-correlations on the temporal velocity signals across the entire field. This is possible because each velocity vector contains a time history for that point in the flow. This was performed by marking as the reference signal the velocity signal at the center of the ensemble-averaged eddy at t=0 μs and cross-correlating this temporal signal with every other velocity vector in the field of view. The results are shown in Fig. 7 for cross-correlations of the u velocity component and in Fig. 8 for the v component. Correlations on the vorticity have been performed as well but, as should be anticipated, they resemble the ensemble averages of Figs. 4 and 5 and hence they are omitted here.

Figure 7 shows that the u component correlates strongly over a region fairly consistent with the size of the characteristic eddy shown in Figs. 4 and 5, possessing an inclination with respect to the coordinate axes. This inclination lies opposite to the jet trajectory. The maximum strength of the correlation decreases as the eddies diffuse and drift from the mean trajectory as they convect downstream. A weak anti-correlation can be seen upstream and downstream of the primary correlation at a distance that appears consistent with the faint counter-rotating vortices detected by the ensemble averages of Figs. 4 and 5. No sign is detected of the paired vortices at a spacing of 8-10 mm, which can be attributed to the distributed azimuthal orientation of the pairing as was shown in Fig. 6.

The cross-correlations on the v component in Fig. 8 tell a similar story but with larger magnitudes. The correlations here are vertically oriented and cover a greater extent than the u component, but still decrease in magnitude as the eddies convect downstream though not as sharply as the loss of u correlation strength in Fig. 7. The most striking difference with Fig. 7 is that Fig. 8 shows the anti-correlations much more distinctly. Both upstream and downstream of the primary correlation, at a distance of 25-30 mm, anti-correlation regions are clearly defined with magnitudes of significant strength, and they maintain their strength even as the primary correlations weaken downstream. Figures 8a and 8f even show a faint positive correlation leading and trailing the anti-correlations by a similar distance. Coupled with the ensemble averages of Figs. 4 and 5, these provide additional evidence that counter-rotating vortices tend to appear in the flow but are not the obvious paired vortices at a distance of 8-10 mm seen in Fig. 3. Yet the strongest anti-correlation is only about 0.25, which indicates that these counter-rotating paired vortices do not occur reliably and may vary somewhat in position, leading to the weakness of the anti-correlations.

The J=10.2 data tell essentially the same story, despite the field-of-view being located closer to the jet core, and hence are supplied here in abbreviated form. A short sequence of velocity fields is shown in Fig. 9, though only four frames are given this time. Many more turbulent eddies are found than at J=8.1, which complicates the visual interpretation of the flowfield. Still, a tendency for paired counter-rotating eddies at a separation of about 10 mm is illustrated by these vector fields. This is most evident in the strong pair that enters the field of view in Fig. 9a at about y=98 mm and convects downstream in subsequent frames. Careful scrutiny suggests additional paired vortices, but the greater prevalence of turbulent eddies of both signs makes visual analysis ambiguous.

Conditional averages of the J=10.2 data look identical to those of the J=8.2 data in Figs. 4 and 5, except that the vorticity magnitudes are slightly larger and the characteristic eddies follow a different trajectory. Replotting with a constant velocity scale and reduced vorticity scale as in Fig. 6 also is quite similar, revealing weak counter-rotating vortices leading and trailing the characteristic vortex by 25-30 mm and a smudge of elevated vorticity at about 10 mm from the characteristic vortex corresponding to the paired turbulent eddies. The consistency of the J=8.1 and J=10.2 ensemble-averaged vortices indicates that the same characteristic behavior of turbulent eddies is found nearer to the jet core despite their greater quantity. The J=10.2 ensemble-average plots are omitted due to their strong resemblance to those already presented at J=8.1.

Cross-correlations also were performed on the J=10.2 data and are given in Figs. 10 and 11 for the u and v components, respectively. Again, the similarity with the J=8.1 data in Figs. 7 and 8 is evident. However, the correlation strength is found to be weaker for J=10.2. As time progresses, the strength of the correlation falls with downstream distance at a faster rate than for J=8.1, and this is true for both the u and v components. Moreover, the anti-correlations are noticeably weaker as well. In the u component they have almost entirely disappeared; in v they are still distinct but the maximum correlation level is mildly diminished in comparison with J=8.1. These reduced correlation levels may be a reflection of increased turbulent activity nearer the core of the jet plume, where the greater quantity of turbulent structures as witnessed in Fig. 9 masks any ordered progression of eddies to a larger extent.

The tendency for turbulent eddies to occur in repeatably-spaced counter-rotating pairs suggests that a characteristic frequency ought to be observed in spectra of the velocity fluctuations. One of the most powerful contributions of pulse-burst PIV is the ability to measure velocity frequency spectra across an entire field of view.

In the present case, however, the properties of the jet interaction change very little across the present field of view and it suffices to examine the spectra at two points. Figure 12 shows the power spectral density (PSD) at two points, one at the mean location of a turbulent eddy upstream (i.e., its position in Figs. 4a and 5a) and another downstream (Figs. 4f and 5f). These points are different for J=8.1 and 10.2, reflecting the differing mean trajectories. Also included are data acquired at twice the acquisition rate, 50 kHz, by double-exposing particle images on a single frame and interrogating images using auto-correlations [5]. This is accomplished at a penalty of poorer spatial resolution and increased uncertainty. Two PSD plots are shown, one for streamwise component of velocity fluctuations and the other for the vertical component.

The PSD's of the streamwise component in Fig. 12a show approximately flat spectra prior to the rolloff at higher frequencies, but the vertical component PSD's in Fig. 12b display a distinct peak. The peaks of the power spectra in Fig. 12b reside at about 4 - 5 kHz with no appreciable difference between the upstream and downstream locations or significant difference as a function of J. Previous studies to examine spectra of jet-in-crossflow velocity fluctuations typically have been intended to measure instability frequencies in the near-field [11, 16, 32, 33], but others show spectra further downstream of the streamwise component [23], the spanwise component [26], and the turbulent kinetic energy [22], all of which resemble those of Fig. 12a. No known previous study detected a frequency peak as in Fig. 12b, but neither did any of the known studies publish results from the vertical velocity component.

At high frequencies, the correlation noise of the cross-correlated data becomes evident at about 8 kHz and appears to initiate a noise floor, whereas the higher-frequency noise in the auto-correlated data appears at about 15 kHz and continues a trend of diminishing energy as frequency rises. It is well-known that the velocity power spectra should obey a power-law dependency of -5/3 once the intertial subrange of turbulence scales is reached (e.g., Pope [31]). However, in the present case this regime is unlikely to have been reached by the current temporal capability. A rough estimate based on Kolmogorov scaling indicates the expected onset of the -5/3 slope would be above 20 kHz; adapting the simulations of Kawai and Lele [22] suggests about 30 kHz.

The peak frequency in Fig. 12b roughly corresponds to a distance of 55 – 70 mm, assuming a convection velocity equivalent to the freestream velocity. In reality, the convection velocity within the jet plume will be a little slower than this so the corresponding distances will be a little shorter as well. The separation between vortices of opposite rotation in the ensemble averages of Fig. 6 and the distance between positive and negative correlation peaks in Figs. 8 and 10 were found to be 25 – 30 mm. Therefore a full period, that is, the separation between vortices of identical sign, is about 50 – 60 mm. This corresponds passably well to the peak frequency observed in the PSD's of Fig. 12b, suggesting that the tendency towards orderly passage of vortex pairs is identifiable in the frequency content of the flowfield.

However, it is not obvious whether the vector fields have detected large-scale vortices within the jet plume that would resemble those found by Ben-Yakar et al [20] or Takahashi et al [21], which suggested structures roughly two jet diameters in size along the windward mixing layer, or VanLerberghe et al [25] whose structures were approximately half that. Computations by Watanabe et al [23] and Peterson and Candler [24] are consistent with these experimental observations. But the apparent structure size is dependent upon the means of measurement. The aforementioned studies used schlieren and planar laser-induced fluorescence to qualitatively image the jet mixing. Comparisons of the present velocity fields to these imaging methods contain considerable ambiguity. Figures 4 and 5 suggest eddies on the order of 5 - 10 mm, depending on whether the velocity vectors or vorticity field is examined. This corresponds to about 0.5 - 1.0 jet diameters, which is smaller than those found using conventional PIV in the same flowfield [7]; the poorer spatial resolution of the earlier experiment effectively acts as a low-pass filter and may explain the discrepancy. The cross-correlations of Figs. 7, 8, 10, and 11 suggest coherent eddies that are easily two jet diameters in extent and perhaps larger. In an imprecise sense, the presently detected vortices do bear some similarity to earlier measurements. However, a more rigorous comparison is not feasible because the present data were collected farther downstream than comparative experiments, and moreover the jet is overexpanded rather than underexpanded, which alters the shock structure at the nozzle exit. Values of J differ as well. An exception is Chai and Mahesh [27], who computed the present flowfield but have not published analysis suitable to a comparison with the present data.

Conclusions

Pulse-burst PIV has been employed to acquire time-resolved data at 25 kHz of a supersonic jet exhausting into a subsonic compressible crossflow. This variant of TR-PIV is necessary to obtain the temporal component of the velocity field in a high-speed ground testing facility. Data were acquired along the windward boundary of the jet mixing layer with the freestream and can be used to identify the turbulent eddies as they convect downstream in the

far-field of the interaction. Conditional ensemble averages, cross-correlations, and spectral analysis were used to analyze the measurements.

Turbulent eddies were found to have a tendency to occur in closely-spaced counter-rotating pairs and are routinely observed in the PIV movies, but the variable orientation of these pairs plus interactions between different eddies makes them difficult to detect in a statistical sense. On a larger spacing, about three times the separation between pairs of eddies, the passage of correlated counter-rotating vortices are more strongly observed. As a turbulent eddy convects through the shear layer, correlated eddies of opposite sign commonly pass by at this spacing both leading and trailing the reference eddy. Taken together, these data indicate the paired nature of the turbulent eddies and the tendency for these pairs to convect through the field of view at uniform spacings. Velocity spectra reveal a peak at a frequency consistent with this larger spacing between shear-layer vortices rotating with identical sign. The spatial scale of these vortices appears similar to previous observations of compressible jets in crossflow.

References

[1] Wernet, M., "Temporally Resolved PIV for Space-Time Correlations in Both Cold and Hot Jet Flows," *Measurement Science and Technology*, Vol. 18, No. 5, 2007, pp. 1387-1403.

[2] Brock, B., Haynes, R. H., Thurow, B. S., Lyons, G., and Murray, N. E., "An Examination of MHz Rate PIV in a Heated Supersonic Jet," AIAA Paper 2014-1102, January 2014.

[3] Miller, J. D., Michael, J. B., Slipchenko, M. N., Roy, S., Meyer, T. R., and Gord, J. R., "Simultaneous High-Speed Planar Imaging of Mixture Fraction and Velocity using a Burst-Mode Laser," *Applied Physics B*, Vol. 113, 2013, pp. 93-97.

[4] Miller, J. D., Gord, J. R., Meyer, T. R., Slipchenko, M. N., Mance, J. G., and Roy, S., "Development of a Diode-Pumped, 100-ms Quasi-Continuous Burst-Mode Laser for High-Speed Combustion Diagnostics," AIAA Paper 2014-2524, June 2014.

[5] Beresh, S. J., Kearney, S. P., Wagner, J. L., Guildenbecher, D. R., Henfling, J. F., Spillers, R. W., Pruett, B. O. M., Jiang, N., Slipchenko, M., Mance, J., and Roy, S., "Pulse-Burst PIV in a High-Speed Wind Tunnel," AIAA paper to be presented at the Science and Technology Forum, Kissimmee, FL, January 2015.

[6] Beresh, S. J., Henfling, J. F., Erven, R. J., and Spillers, R. W., "Penetration of a Transverse Supersonic Jet into a Subsonic Compressible Crossflow," *AIAA Journal*, Vol. 43, No. 2, 2005, pp. 379-389.

[7] Beresh, S. J., Henfling, J. F., Erven, R. J., and Spillers, R. W., "Turbulent Characteristics of a Transverse Supersonic Jet in a Subsonic Compressible Crossflow," *AIAA Journal*, Vol. 43, No. 11, 2005, pp. 2385-2394.

[8] Beresh, S. J., Henfling, J. F., Erven, R. J., and Spillers, R. W., "Crossplane Velocimetry of a Transverse Supersonic Jet in a Transonic Crossflow," *AIAA Journal*, Vol. 44, No. 12, 2006, pp. 3051-3061.

[9] Karagozian, A. R., "Transverse Jets and their Control," *Progress in Energy and Combustion Science*, Vol. 36, No. 5, 2010, pp. 531-553.

[10] Mahesh, K., "The Interaction of Jets with Crossflow," *Annual Review of Fluid Mechanics*, Vol. 45, 2013, pp. 379-407.

[11] Fric, T. F., and Roshko, A., "Vortical Structure in the Wake of a Transverse Jet," *Journal of Fluid Mechanics*, Vol. 279, 1994, pp. 1-47.

[12] Kelso, R. M., Lim, T. T., and Perry, A. E., "An Experimental Study of Round Jets in Cross-flow," *Journal of Fluid Mechanics*, Vol. 306, 1996, pp. 111-144.

[13] Smith, S. H., and Mungal, M. G., "Mixing, Structure and Scaling of the Jet in Crossflow," *Journal of Fluid Mechanics*, Vol. 357, 1998, 83-122.

[14] Su, L. K., and Mungal, M. G., "Simultaneous Measurements of Scalar and Velocity Field Evolution in Turbulent Crossflowing Jets," *Journal of Fluid Mechanics*, Vol. 513, 2004, pp. 1-45.

[15] Meyer, K. E., Pedersen, J. M., and Ozcan, O., "A Turbulent Jet in Crossflow Analysed with Proper Orthogonal Decomposition," *Journal of Fluid Mechanics*, Vol. 583, 2007, pp. 199-227.

[16] Megerien, S., Davitian, J., Alves, L. S. de B., and Karagozian, A. R., "Transverse-Jet Shear-Layer Instabilities. Part 1. Experimental Studies," *Journal of Fluid Mechanics*, Vol. 593, 2007, pp. 93-129.

[17] Getsinger, D. R., Gevorkyan, L., Smith, O. I., and Karagozian, A. R., "Structural and Stability Characteristics of Jets in Crossflow," *Journal of Fluid Mechanics*, Vol. 760, 2014, pp. 342-367.

[18] Alves, L. S. de B., Kelly, R. E., and Karagozian, A. R., "Transverse-Jet Shear-Layer Instabilities. Part 2. Linear Analysis for Large Jet-to-Crossflow Velocity Ratio," *Journal of Fluid Mechanics*, Vol. 602, 2008, pp. 383-401.

[19] Gruber, M. R., Nejad, A. S., Chen, T. H., and Dutton, J. C., "Compressibility Effects in Supersonic Transverse Injection Flowfields," *Physics of Fluids*, Vol. 9, No. 5, 1997, pp. 1448-1461.

[20] Ben-Yakar, A., Mungal, M. G., and Hanson, R. K., "Time Evolution and Mixing Characteristics of Hydrogen and Ethylene Transverse Jets in Supersonic Crossflows," *Physics of Fluids*, Vol. 18, No. 2, 2006, pp. 026101.

[21] Takahashi, H., Masuya, G., and Hirota, M., "Effects of Injection and Main Flow Conditions on Supersonic Turbulent Mixing Structure," *AIAA Journal*, Vol. 48, No. 8, 2010, pp. 1748-1756.

[22] Kawai, S., and Lele, S. K., "Large-Eddy Simulation of Jet Mixing in Supersonic Crossflows," *AIAA Journal*, Vol. 48, No. 9, 2010, pp. 2063-2083.

[23] Watanabe, J., Kouchi, T., Takita, K., and Masuya, G., "Numerical Study on the Turbulent Structure of Transverse Jet into Supersonic Flow," *AIAA Journal*, Vol. 49, No. 9, 2011, pp. 2057-2067.

[24] Peterson, D. M., and Candler, G. V., "Simulations of Mixing for Normal and Low-Angled Injection into Supersonic Crossflow," *AIAA Journal*, Vol. 49, No. 12, 2011, pp. 2792-2804.

[25] VanLerberghe, W. M., Santiago, J. G., Dutton, J. C., Lucht, R. P., "Mixing of a Sonic Transverse Jet Injected into a Supersonic Flow," *AIAA Journal*, Vol. 38, No. 3, 2000 pp. 470-479.

[26] Genin, F., and Menon, S., "Dynamics of Sonic Jet Injection into Supersonic Crossflow," *Journal of Turbulence*, Vol. 11, No. 4, 2010, pp. 1-30.

[27] Chai, X., and Mahesh, K., "Simulations of High Speed Turbulent Jets in Crossflows," AIAA Paper 2011-650, January 2011.

[28] Slipchenko, M. N., Miller, J. D., Roy, S., Gord, J. R., Danczyk, S. A., and Meyer, T. R., "Quasi-Continuous Burst-Mode Laser for High-Speed Planar Imaging," *Optics Letters*, Vol. 37, No. 8, pp. 1346-1348, 2012.

[29] Slipchenko, M. N., Miller, J. D., Roy, S., Gord, J. R., and Meyer, T. R., "All-Diode-Pumped Quasi-Continuous Burst-Mode Laser for Extended High-Speed Planar Imaging," *Optics Express*, Vol. 21, No. 1, pp. 681-689, 2013.

[30] Slipchenko, M. N., Miller, J. D., Roy, S., Meyer, T. R., Mance, J. G., and Gord, J. R., "100-kHz, 100-ms, 400-J Burst-Mode Laser with Dual-Wavelength Diode Amplifiers," *Optics Letters*, accepted for publication, 2014.

[31] Pope, S. B., *Turbulent Flows*, Cambridge University Press, 2000, pp. 228-239.

[32] Moussa, Z. M., Trischka, J. W., and Eskinazi, S., "The Near Field in the Mixing of a Round Jet with a Cross-Stream," *Journal of Fluid Mechanics*, Vol. 80, Part 1, 1977, pp. 49-80.

[33] Andreopoulos, J., "On the Structure of Jets in a Crossflow," *Journal of Fluid Mechanics*, Vol. 157, 1985, pp. 163-197.

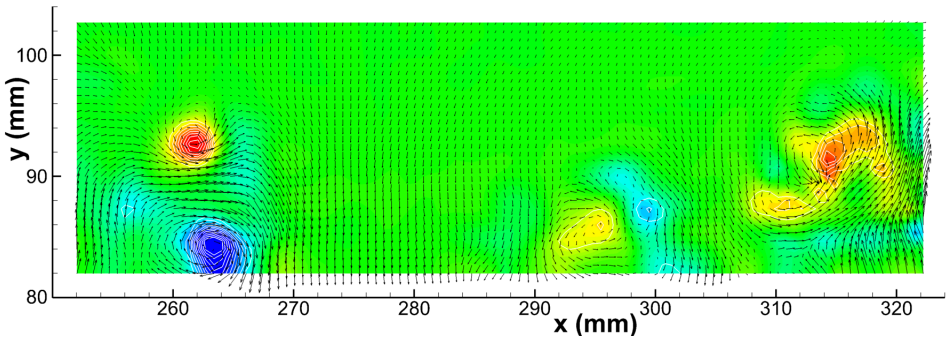

(a): t = 0 μs

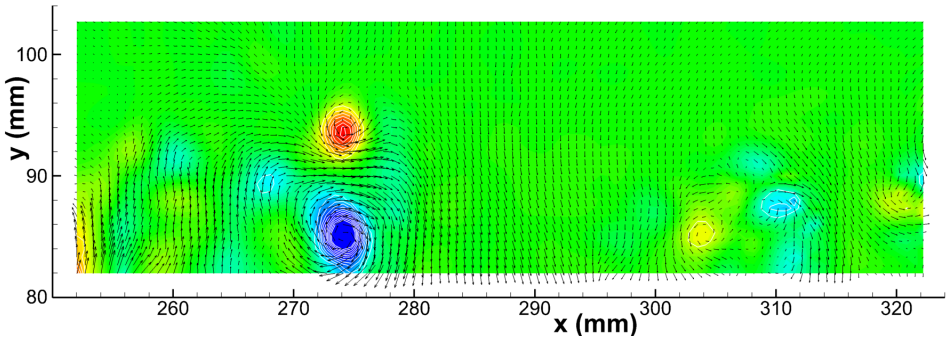

(b): t = 40 μs

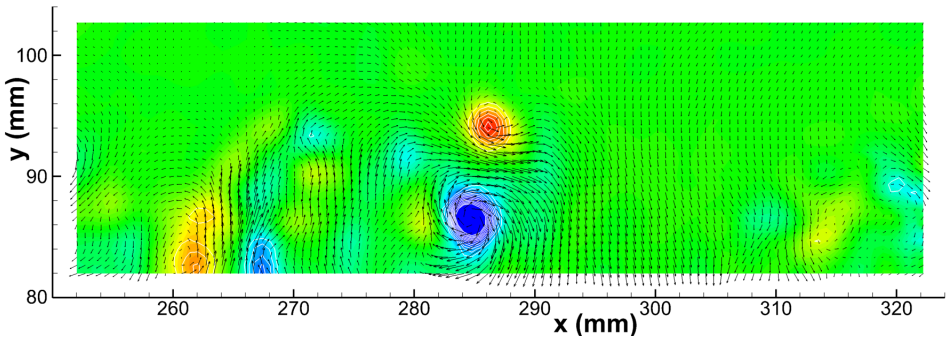

(c): t = 80 μs

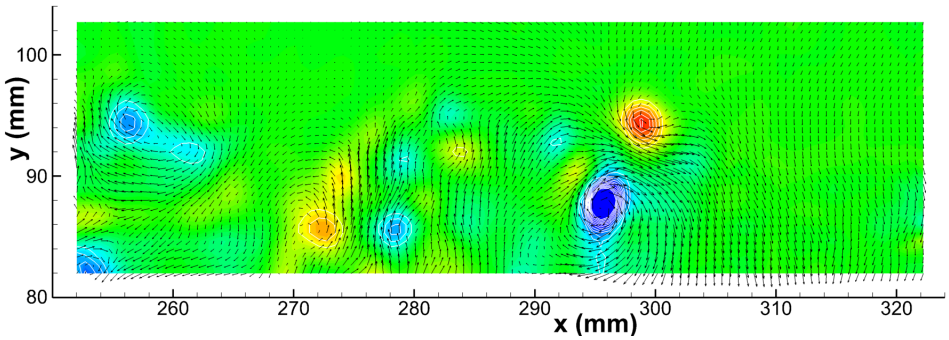

(d): t = 120 μs

Fig. 3: Sequence of eight velocity fields extracted from a 2.5 ms burst of 58 velocity fields, acquired for a Mach 3.7 jet issuing into a Mach 0.8 crossflow at J=8.1. Vectors show the in-lane velocity fluctuations superposed on a color contour plot of the derived vorticity field and white line contours of the swirl field. Each snapshot is separated by 40 μs. Continued on next page.

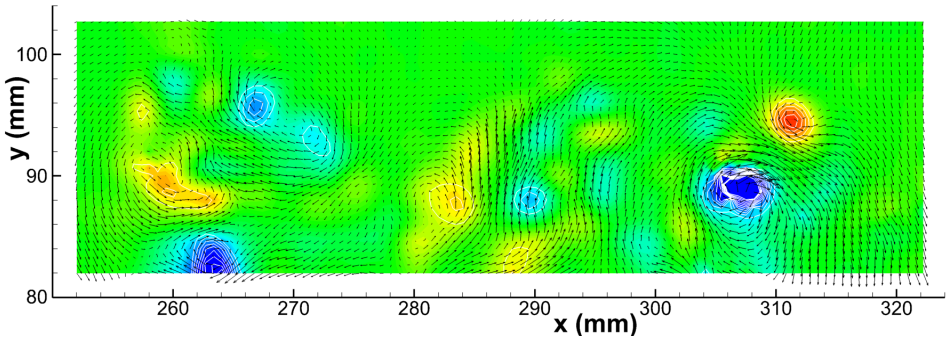

(e): t = 160 μs

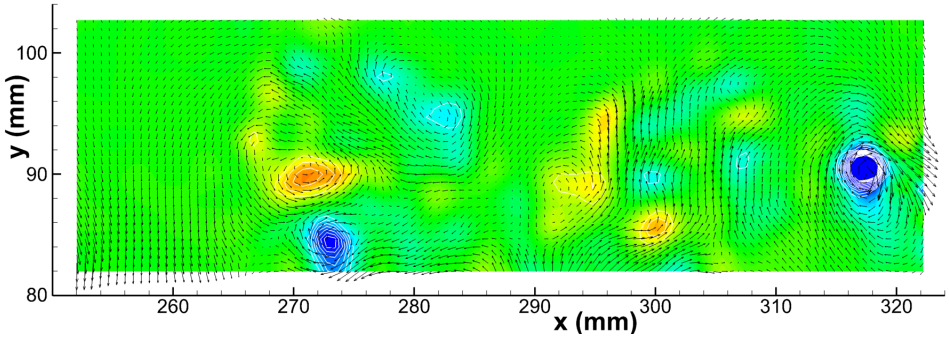

(f): t = 200 μs

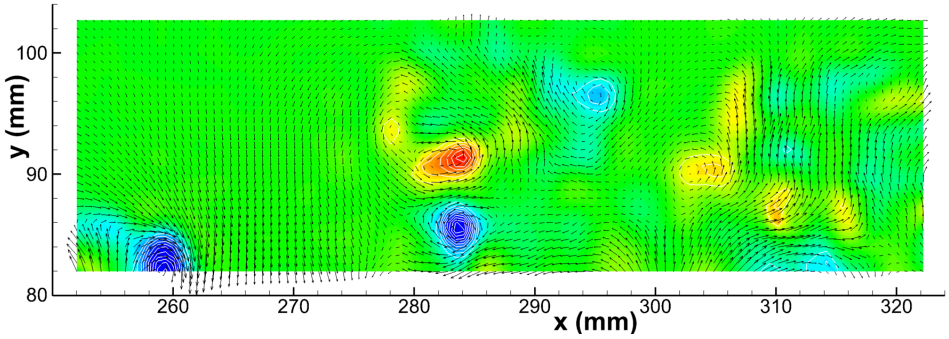

(g): t = 240 μs

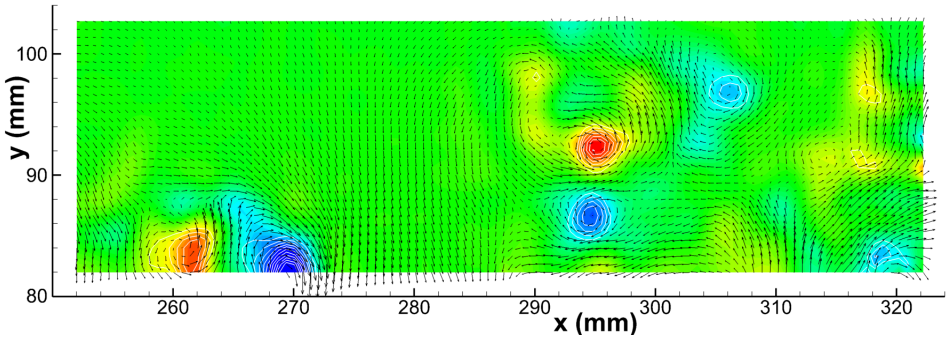

(h): t = 280 μs

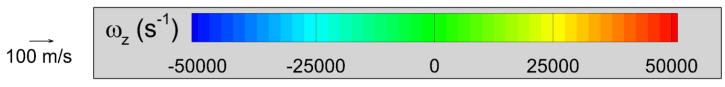

Fig. 3: Continued from previous page.

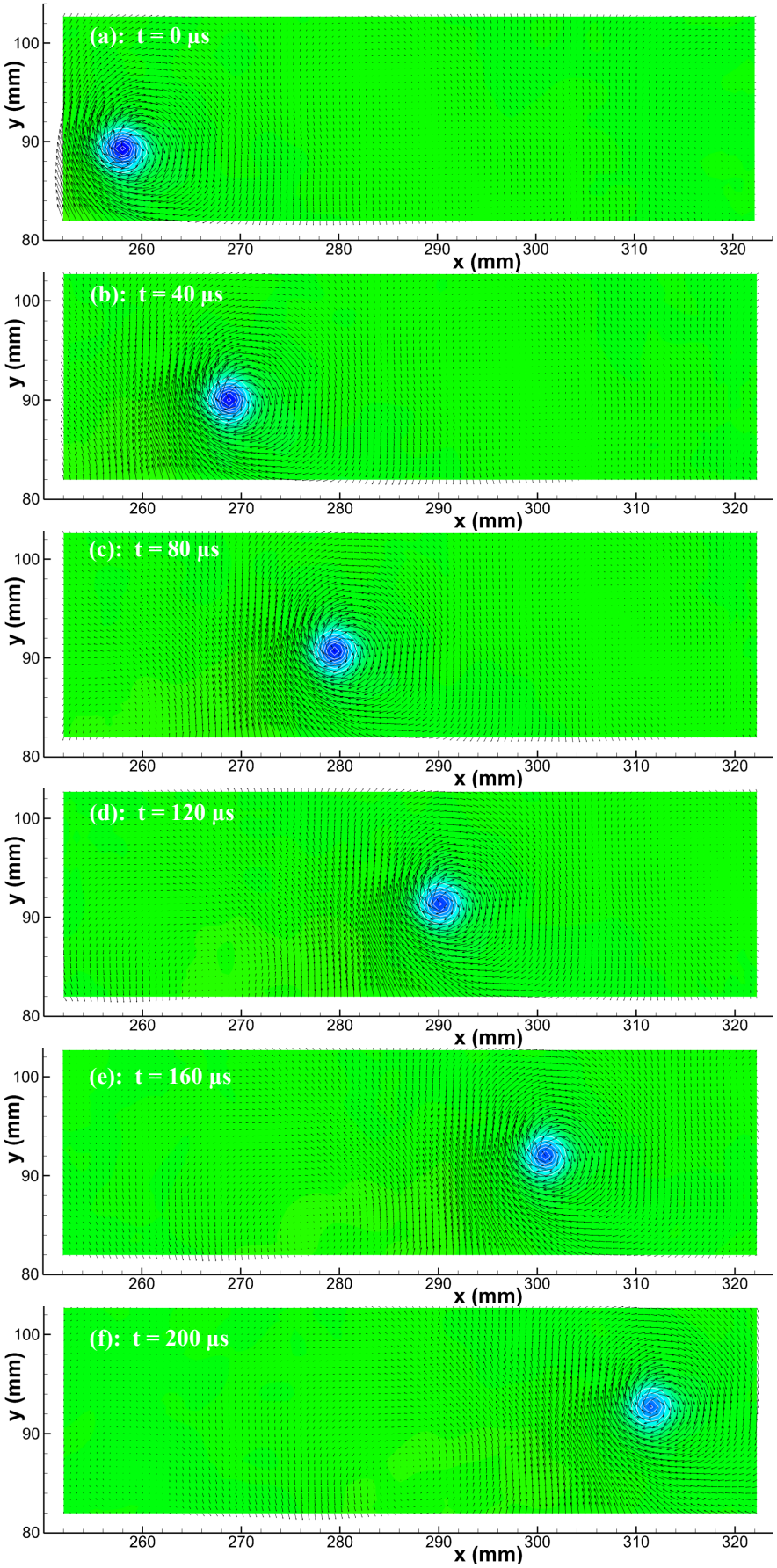

Fig. 4: Sequence of ensemble-averaged velocity fields of the evolution of a characteristic turbulent eddy, conditioned on a negative-rotating eddy. J=8.1. Same velocity and vorticity scale as Fig. 3.

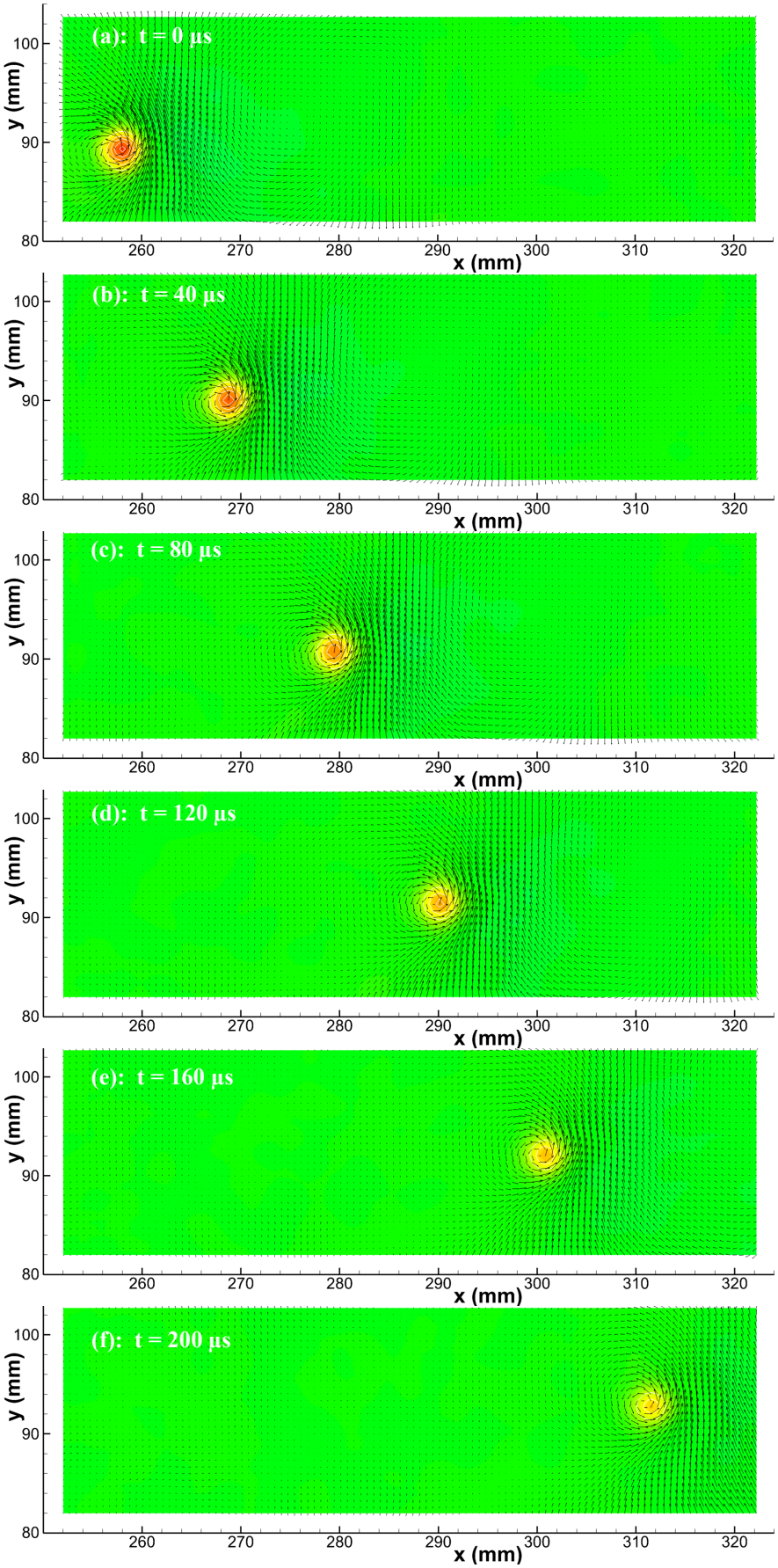

Fig. 5: As Fig. 4, but conditioned on a positive-rotating eddy.

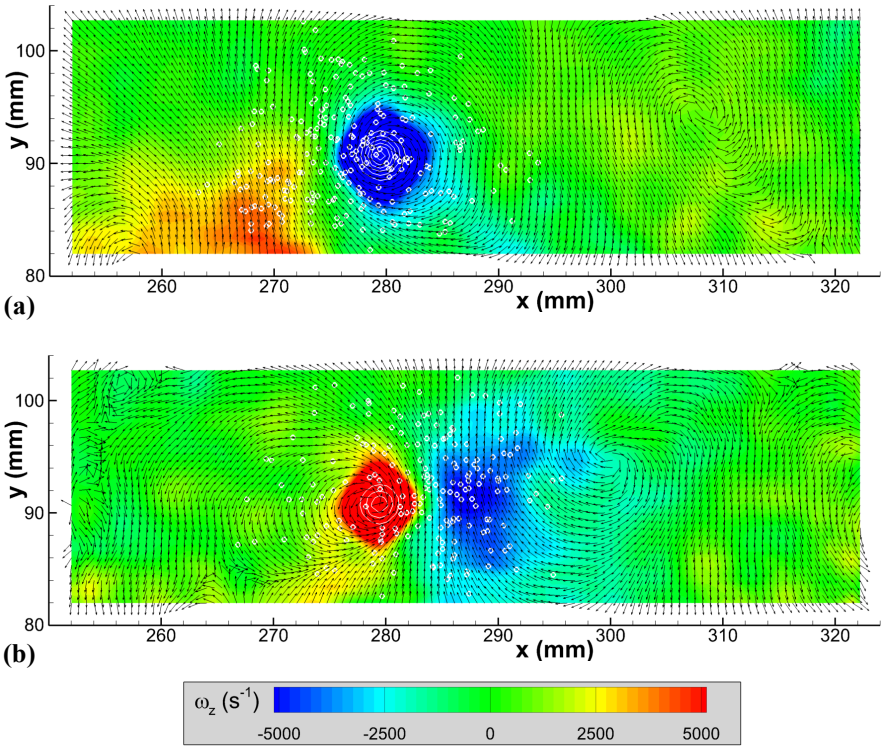

Fig. 6: Ensemble-averaged velocity fields at t=80 μs of characteristic turbulent eddy, with constant length velocity vectors and reduced vorticity scale. J=8.1. (a) negative rotating eddy; (b) positive rotating eddy.

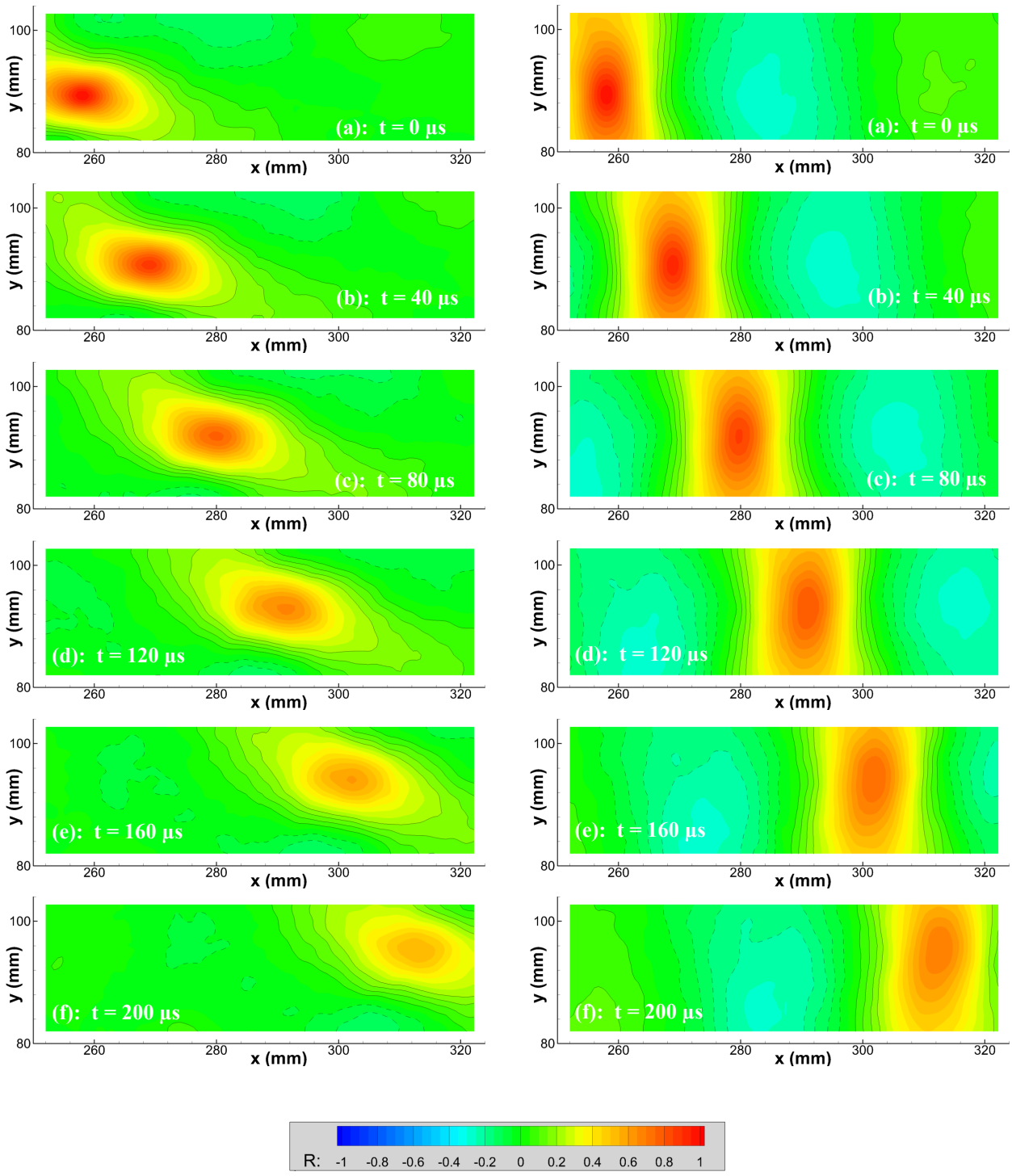

Fig. 7: Sequence of temporal cross-correlations of the streamwise velocity component with reference point at the center of the t=0 ensemble-averaged vortex. Line contours emphasize the correlation level at intervals of 0.05 in the range of ±0.2, with dashed line for anti-correlations. J=8.1.

Fig. 8: As Fig. 5, but for the vertical velocity component.

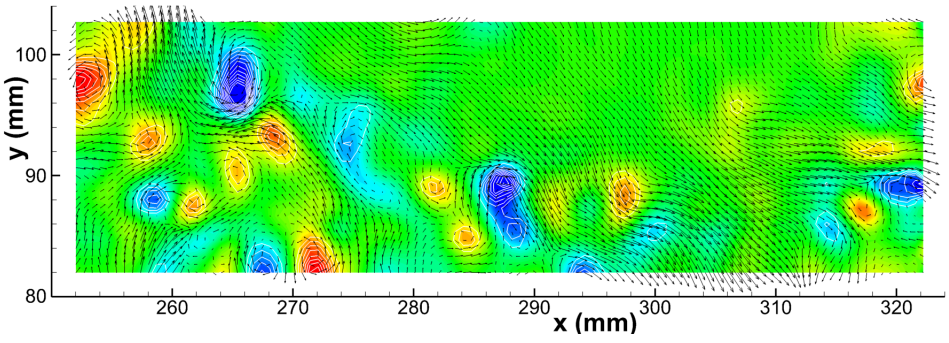

(a): t = 0 μs

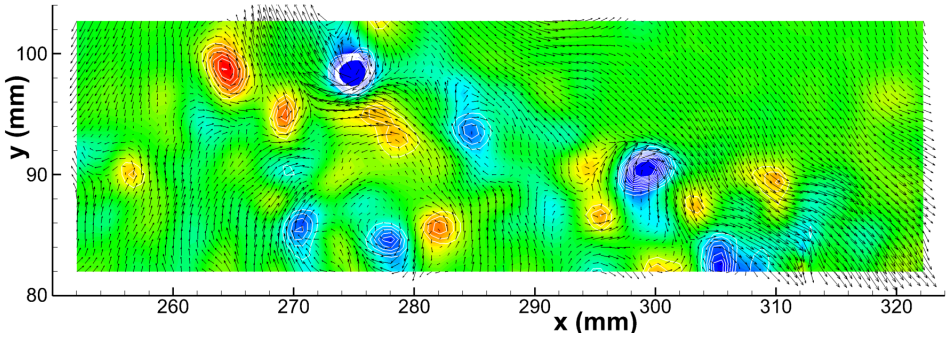

(b): t = 40 μs

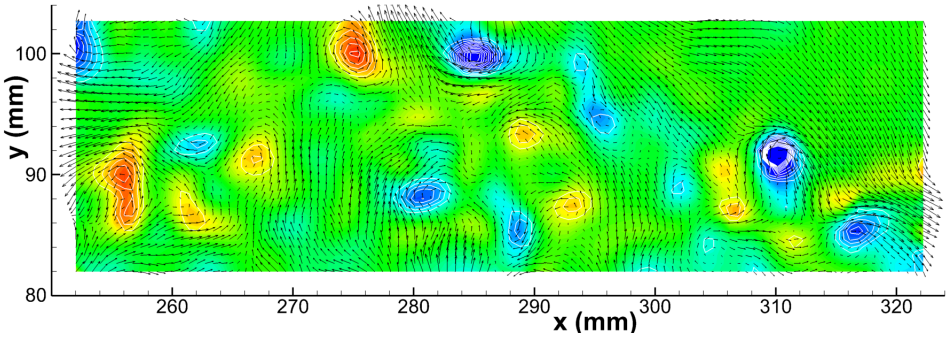

(c): t = 80 μs

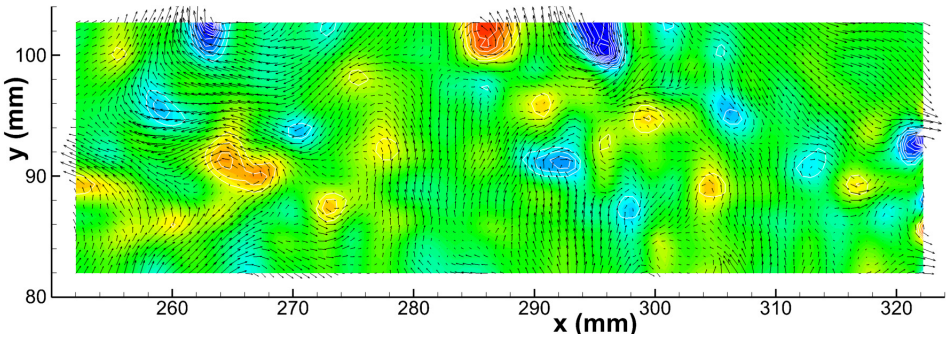

(d): t = 120 μs

Fig. 9: As Fig. 3 but a sequence of four vector fields at J=10.2.

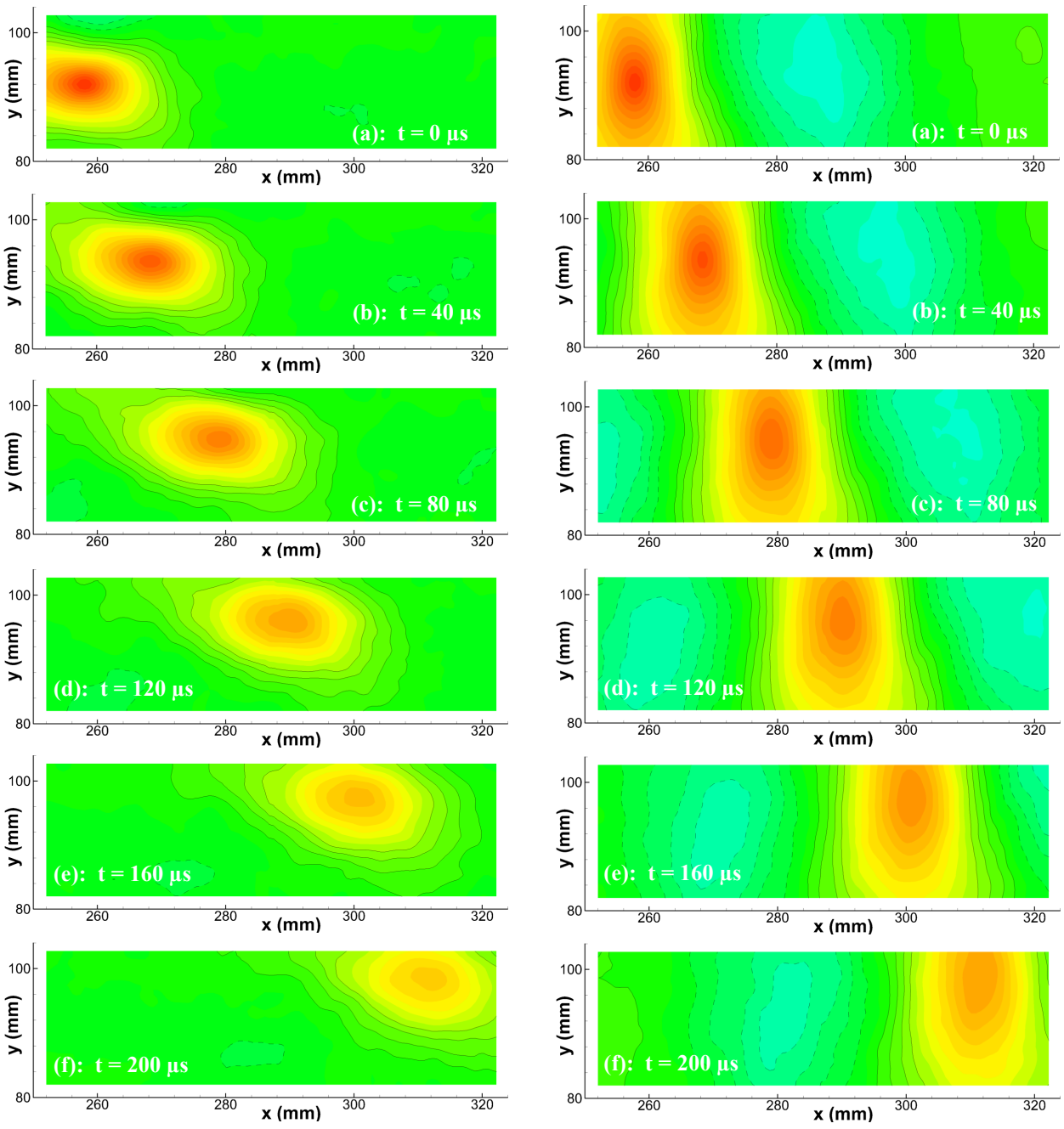

Fig. 10: Cross-correlations of the streamwise velocity component as Fig. 7, but J=10.2.

Fig. 11: As Fig. 10, but for the vertical velocity component.

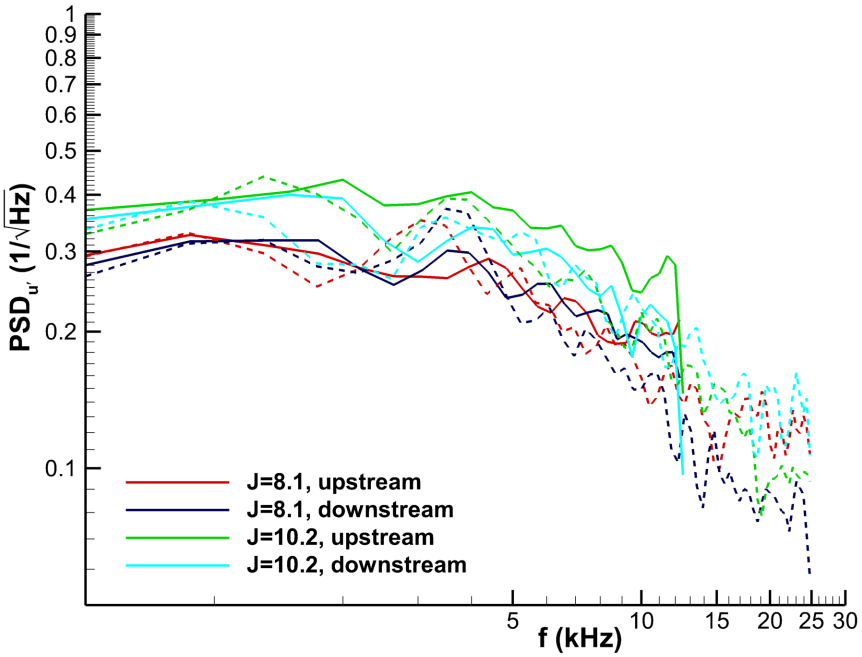

(a)

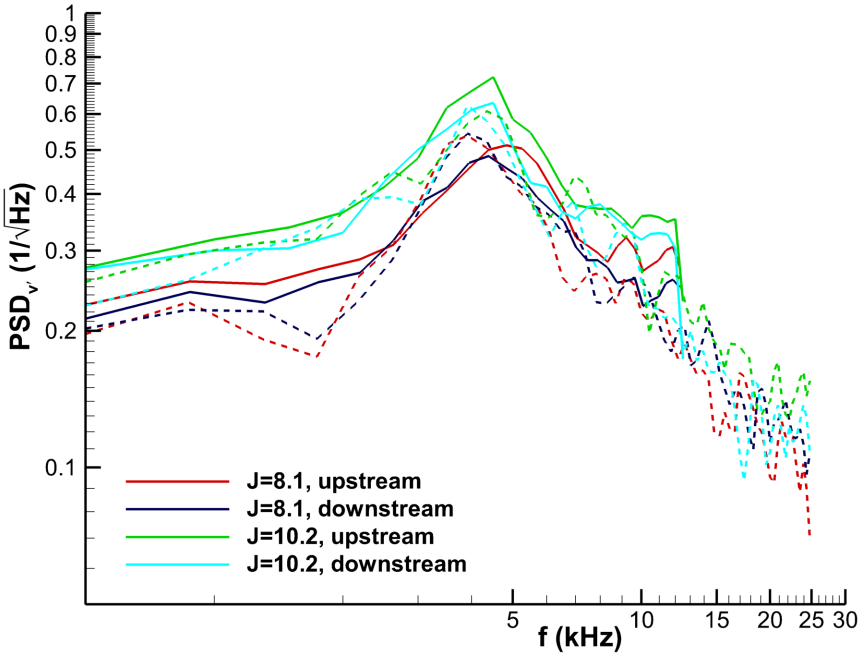

(b)

Fig. 12: Power spectra of velocity fluctuations found in the jet in crossflow at J=8.1 and J=10.2, measured at an upstream location in the field of view and a downstream location. Solid lines denote cross-correlation data at 25 kHz and broken lines denote auto-correlation data at 50 kHz. (a) streamwise component; (b) vertical component.